The regulation of multistep spin-crossover across multiple stimuli in a 2-D framework material

Manan Ahmed, Katrina A. Zenere, Natasha F. Sciortino, Kasun S. A. Arachchige, Gemma F. Turner, Jace Cruddas, Carol Hua, Jason R. Price, Jack K. Clegg, Francisco Javier Valverde-Muñoz, Jose A. Real, Guillaume Chastanet, Stephen A. Moggach, Cameron J. Kepert,* Benjamin J. Powell,* Suzanne M. Neville*

S1. Synthesis and characterisation

General Procedures

All materials were available commercially and used as received (iron(II) perchlorate was handled carefully and in small amounts to avoid any potential explosions). Metal cyanides are toxic and should be used with care and in small amounts.

Synthesis of (1*E*,2*E*)-3-phenyl-*N*-(4*H*-1,2,4-triazol-4-yl)prop-2-en-1-imine (cintrz)

The ligand cintrz was prepared by literature methods.[1] Cinnamaldehyde 1.35 g (10 mmol) and 4-amino-1,2,4-triazole 0.84 g (10 mmol) were dissolved in 50 mL ethanol and refluxed 4 h with a catalytic amount of conc. sulfuric acid. The crude product was obtained as a white powder with addition of cold ice water to the solution. The precipitate was filtered and washed with water followed by *n*-hexane. The crude product recrystallized from hot ethanol yielded off-white needle-shaped crystals of cintrz (Yield: 1.62 g, 82.3 %). ^{1}H NMR (400 MHz, d_6-DMSO, ppm): δ = 9.06 (s, 2H), 8.84 (d, 1H), 7.72-7.70 (dd, 2H), 7.47-7.32 (m, 4H) 7.20-7.13 (q, 1H). ^{13}C NMR: δ = 159.68, 145.48, 138.86, 134.92, 130.17, 129.04, 127.92, 123.57. IR (cm^{-1}): 1629 (s), 1586 (w), 1496 (s), 1448 (w), 1291 (w), 1170 (s), 1052 (s), 995 (vw), 979 (s), 937 (m), 878 (w), 840 (m), 751 (s), 673 (s), 632 (w), 620 (s), 512 (m), 487 (m). Elemental analysis calculated for $C_{11}H_{10}N_4$ (%): C 66.65; N 28.26; H 5.09; Found (%): C 66.13; N 28.28; H 5.56. ESI-MS (ESI$^+$, m/z): calculated for $[M+H]^+$ $C_{11}H_{10}N_4$ 198.09, Found 199.08. Melting point: 190.1 °C.

Synthesis of $[Fe(cintrz)_2Pd(CN)_4]\cdot 3H_2O$ (A·3H$_2$O)

Bright-yellow square plate single crystals of complexes were synthesized by slow diffusion of $Fe(ClO_4)_2\cdot xH_2O$ (0.08 mmol, 20.1 mg) into cintrz (0.16 mmol, 32 mg) and $K_2[Pd(CN)_4]\cdot xH_2O$ (0.08 mmol, 23.0 mg) in a 1:1 mixture of EtOH: H_2O using the vial-in-vial method. In this method, $Fe(ClO_4)_2\cdot xH_2O$ charged in a small vial and cintrz and $K_2[Pd(CN)_4]\cdot xH_2O$ in a large vial. The small vial was inserted into the large vial and carefully filled with EtOH: H_2O mixture to avoid distributing the reactants and sealed. The vials were left undisturbed and after *ca*. 4 weeks yellow single crystals of **A**·3H$_2$O formed (yield: 63%). Elemental anal. calcd for $FePdC_{26}H_{20}N_{12}\cdot 3H_2O$ (%): C, 43.56; H, 3.66; N, 23.45. Found (%): C, 44.10; H, 3.34; N, 23.78. IR bands (cm^{-1}): 2167(m), 1626(m), 1587(vs), 1510(s), 1449(vs), 1171(m), 1058(m), 986(s), 752(m), 689(vs), 615(s). A bulk crystalline sample of $[Fe(cintrz)_2Pd(CN)_4]\cdot 2H_2O$ (**A**·2H$_2$O) was prepared by leaving a sample of **A**·3H$_2$O exposed to air for 24h. A bulk crystalline sample of $[Fe(cintrz)_2Pd(CN)_4]$ (**A**·∅) was prepared by heating **A**·3H$_2$O to 100 °C for 24 h.

General physical measurements

Fourier transform infra-red (FT-IR) spectra were recorded in transmission mode with Thermo-Fisher ATR Nicolet-iS5 spectrometer equipped with a smart iD7 diamond window in the range of 400-4000 cm^{-1}, with 64 scans and a resolution of 4 cm^{-1}. Elemental analyses (carbon, hydrogen, and nitrogen) were performed at the Campbell Microanalytical Laboratory, University of Otago. ^{1}H and ^{13}C NMR spectra were recorded on Bruker 400 MHz NMR spectrometer equipped with an autosampler (d_6-DMSO). Chemical shifts are reported in ppm with internal TMS standard. A thermo-Fisher mass spectrometer (m/z 50-2000) was used under a positive ion mode with the ESI source using methanol as eluent. Melting point was determined via an OptiMelt (SRS MPA 100) melting point apparatus in an open borosilicate capillary tube.

Thermogravimetric analysis (TGA)

TGA were performed on a Mettler Toledo instrument in the temperature range of 30 - 400 °C under a nitrogen atmosphere (flow rate: 10 mL/min) with a heating rate of 1 K/min. The samples were held at 30 °C for 30 min to stabilize the initial temperature and then heated from 30 to 400 °C. The sample was corrected for buoyancy effect by subtracting the measured TGA for an empty crucible using the same experimental protocol. Figures S1-2 show the TGA data for **A**·3H$_2$O and **A**·2H$_2$O, both showing mass loss up to 150 °C from the evolution of the respective guest molecules, followed by stability of the empty framework and then framework decomposition.

Differential scanning calorimetry (DSC)

Differential scanning calorimetry (DSC) measurements were carried out using Netzsch DSC 204 F1 phoenix calorimeter equipped with an external liquid nitrogen cryostat. Microcrystalline samples (10-14 mg) were used and sealed in an aluminium pan with a mechanical crimp - an empty pan was used as a reference. Data were collected over the 220 -160 - 220 K range with a scan rate of 10 K/min. Pure nitrogen was used as a purge gas (flow rate: 20 mL/min) to avoid water condensation. Netzsch Proteus Analysis software was used for data analyses. Figures S3-4 show the DSC data for **A**·$3H_2O$ and **A**·$2H_2O$, showing endothermic and exothermic peaks corresponding to the spin-state transitions. These peaks are coincident with the SCO transition temperatures recorded by temperature-dependent magnetic susceptibility. We note that only the higher temperature [HS-HS] to [HS-LS] step for **A**·$2H_2O$ was able to be recorded, the lower temperature step ([HS-LS] to [LS-LS]) occurs outside the temperature range of the equipment.

Magnetic susceptibility

Temperature-dependent magnetic susceptibility data were collected on a Quantum Design Versalab magnetometer, fitted with a vibrating sample magnetometer (VSM), under an applied magnetic field of 0.3 T. Measurements were taken continuously in sweep mode at a scan rate of 0.5, 1, 2 and 4 K/min. To prevent solvent loss, a specialized sample holder was constructed. The samples were loaded into a hollow perfluoroalkoxy (PFA) tube stoppered with a PMMA plug. This was centrifuged such that the samples were firmly packed in the bottom of the tube, and excess solvent was removed. A small amount of cotton wool was inserted to firmly pack the samples, and the sample holders were flame-sealed to prevent solvent loss. Data were collected over the temperature range 300 – 50 – 300 K (Figures S17-18).

Photomagnetic measurements were performed using a Quantum Design MPMS-XL-5 SQUID magnetometer over the temperature range of 2 – 300 K with an applied magnetic field of 2 T. The crystalline sample of **A**·$3H_2O$ was prepared in a thin layer to promote full penetration of the irradiation light.[2-3] The characterization was carried out using a set of photodiodes. Irradiation was carried out at 10 K several times using different wavelength (i.e., 405, 510, 650, 830 and 900) to determine the most efficient condition and once photosaturation was reached, irradiation was ceased. Power intensities of 6 $mW.cm^{-2}$ at 510 nm and 10 $mW.cm^{-2}$ at 830 nm were used for measurement. LIESST experiment was performed using a 510 nm wavelength. After irradiation was switched off, the temperature was increased at a rate of 0.4 K/min up to 100 K, to determine the T(LIESST) value and magnetization was also measured from 100 to 300 to 10 K to follow the thermal spin transition. The T(LIESST) value was determined as the minimum of the $\partial\chi_M T/\partial T$ versus T curve, corresponding to the temperature at which the light-induced HS information is erased in the SQUID cavity.[3-7] Moreover, the reverse-LIESST experiment was performed by irradiating the sample at 10 K in the plateau region with 830 nm diode laser until saturation of the LS was reached. Figure S21 shows the 'on-off' switching achieved via repetitive LIESST and reverse-LIESST experiments. All the experiments performed under or after light irradiation using a scan rate of 0.4 K/min.

Magnetic measurements under pressure were performed on a crystalline sample of **A**·$3H_2O$ using a hydrostatic pressure cell, specially designed for the SQUID set up in the Valencia lab (SQUID specifications: Quantum Design MPMS2 SQUID magnetometer operating at 1 T and 1.8 – 320 K), made of hardened beryllium bronze with silicon oil as the pressure transmitting medium and operating over the pressure range 1 bar – 12 kbar. The compound was packed in a cylindrically shaped sample holder (1 mm in diameter and 5-7 mm in length) made up of very thin aluminium foil. The pressure was calibrated using the transition temperature of a superconducting lead of high-purity 99.999%.

Powder X-ray diffraction

Variable temperature X-ray powder diffraction were collected at the powder diffraction beamline (BL-10) at the Australian Synchrotron.[8] The beamline was set up with a nominal wavelength of 1.0 Å; the wavelength was determined accurately using NIST SRM LaB_6 660b to be 0.999982(2) Å. The samples were loaded into 0.5 mm diameter quartz glass capillaries, which were sealed with wax to prevent solvent loss. The capillaries were rotated (1 Hz) to improve powder averaging. Data were collected using a Mythen II microstrip detector[9] from 3 to 83° in 2θ. To

cover the gaps between detector modules, two data sets were collected with the detector set 0.5° apart and these were then merged to give a single data set using in-house software PDViPER.[10] The sample temperature was controlled using an Oxford Cryosystem 700 Plus. Data were collected at *ca*. 3 K intervals over the range 250 – 100 – 250 K for **A**·3H_2O and 250 – 90 K for **A**·2H_2O. Le Bail and peak fitting analyses of the diffraction data were performed using TOPAS *v*6[11] software. Representative Le Bail fits for **A**·3H_2O and **A**·2H_2O are shown in Figures S5-6, confirming phase identity and purity. Plots of the qualitative and quantitative temperature-dependence of the Bragg peaks are shown in Figures S7-8.

Single crystal X-ray diffraction

Variable temperature single crystal data were recorded on a Rigaku Synergy S diffractometer by using monochromatic Mo-Kα radiation (λ = 0.71073 Å). A selected single crystal was carefully mounted on the nylon loop with paratone-N oil and mounted on the diffractometer. An Oxford cryo-systems temperature controller was used. CrysAlisPro[12] was used for the unit cell determination, data reduction and integration. The structures were solved by a direct method with ShelXT[13] structure solution and refined by full-matrix least-squares on F^2 refinement with ShelXL[14] using the Olex2[15] software package. All non-hydrogen atoms were then refined anisotropically, and hydrogen atoms were placed in idealized positions to the structure and treated as riding atoms. Representative thermal ellipsoid diagrams for **A**·3H_2O and **A**·2H_2O are shown in Figures S9-10, illustrating the atom labelling. Variable temperature unit cell data were also collected, for **A**·3H_2O over the range 200 – 165 – 200 K (at 5 K intervals) and for **A**·2H_2O over the range 250 – 90 – 250 K (at 10 K intervals). Plots of the unit cell volume and parameters versus temperature are shown in Figures S11-12. Crystallographic data and refinement details are provided for two temperatures for **A**·3H_2O representative of the HS-HS and HS-LS states and for three temperatures for **A**·2H_2O representative of the HS-HS, HS-LS and LS-LS states (Fe1-Fe2) in Table S1. Selected structural parameters are given in Table S2.

Photo-induced single crystal single crystal data were recorded on a Rigaku Synergy S diffractometer by using monochromatic Mo-Kα radiation (λ = 0.71073 Å). A selected single crystal was carefully mounted on the nylon loop with paratone-N oil and mounted on the diffractometer. The data was collected in dark and under irradiation of red light on the same crystal at 30 K. An Oxford cryo-systems temperature controller was used. CrysAlisPro[12] was used for the unit cell determination, data reduction and integration. The structures were solved by a direct method with ShelXT[13] structure solution and refined by full-matrix least-squares on F^2 refinement with ShelXL[14] using the Olex2[15] software package. All non-hydrogen atoms were then refined anisotropically, and hydrogen atoms were placed in idealized positions to the structure and treated as riding atoms. The guest molecules excluded from the structure model using the SQUEEZE algorithm in PLATON.[16] Variable temperature unit cell data were also collected after irradiation over the range 30 – 250 K (at 10 K intervals). Plots of the unit cell volume and parameters versus temperature are shown in Figure S13. Crystallographic data and refinement details are provided in Table S3 and selected structural parameters are given in Table S4.

Variable pressure single crystal X-ray diffraction data were collected on **A**·3H_2O. Firstly, a pale yellow, single crystal of **A**·3H_2O was characterised under ambient conditions by single crystal X-ray diffraction, using a Rigaku Synergy-S diffractometer, equipped with graphite-monochromated Mo Kα radiation (λ = 0.7107 Å). Diffraction data were integrated and corrected for absorption effects in CrysAlisPro.[12] The crystal structure was solved using ShelXT[13] and refined using ShelXL[14] in Olex2.[15] All geometric and thermal parameters were refined freely. The occupancy of the free H_2O in the crystal was refined freely, before being constrained to its converged value. All H-atoms were placed geometrically and constrained to ride on their host atoms.

The same crystal of **A**·3H_2O that was collected at ambient pressure was loaded into a modified miniature Merrill-Bassett diamond anvil cell,[17] equipped with a 40° opening angle, 600 μm culet Boehlar-Almax diamond anvils, tungsten carbide backing seats[17] and a pre-indented tungsten gasket. Inert oil, MiTeGen LVCO-5 Cryo OilTM was used as the pressure-transmitting medium. A sphere of ruby was placed in the sample chamber to serve as a pressure calibrant. The pressure within the sample chamber was measured using the ruby fluorescence method.[18] Diffraction data were collected on a Rigaku Oxford Diffraction XtaLAB Synergy-S diffractometer, using Mo Kα radiation (λ = 0.7107 Å) at ambient pressure, 0.14 GPa, 0.36 GPa, 0.57 GPa, 1.01 GPa, 1.72 GPa and 2.75. The data collection strategy was determined by a high-pressure pre-experiment (using ϕ scans from -10 – 10° and 170 – 190°) in CrysAlis Pro.[12] Reflections from the diamond anvils and ruby chip were removed from the diffraction data prior to

integration. Diffraction data were integrated using shading masks and corrected for absorption in CrysAlis Pro.[12] Crystallographic data and refinement details are provided in Table S5 and selected structural parameters are given in Table S6. Table S7 presents the compressibility and bulk modulus data.

Structural degradation of the crystal at 2.75 GPa precluded atomistic refinement at this pressure, allowing on the unit cell dimensions to be measured. The crystal structures at all other pressures were solved using the starting coordinates of either the ambient pressure structure, or the structure collected at the previous pressure point. Structures were refined using ShelXL[14] in Olex2.[15] Bond lengths and 1,3-distances in the cintrz and cyano ligands were restrained to those in the structure model under ambient conditions. Phenyl rings were constrained to hexagonal and restrained to planarity. All metal-ligand bond distances and angles were refined freely. All atoms were refined with isotropic displacement parameters due to the low completeness of the data caused by shading of the detector by the pressure cell. The pore volume was estimated using the SQUEEZE algorithm in PLATON,[16] with the guest molecules excluded from the structure model.

Structural data are reported are freely available via the CCDC under 2129325-2129335.

Elastic model

On making the symmetric breathing mode approximation, that is setting $r_{i,j} = \eta_n x$, where the η_n are constants (defined in the main text) and the average intralayer nearest neighbour metal-metal separation, x, remains variable, we find that

$$H = H_0 + \sum_{n=1}^{m} \frac{k_n}{2} \sum_{\langle i,j \rangle_n} \left(\eta_n x - \eta_n \bar{R} - \eta_n \delta(\sigma_i + \sigma_j) \right)^2 + pL^3 c x^2$$

$$= H_0 + \left[\frac{L^2}{4}(x - \bar{R})^2 - \delta(x - \bar{R}) \sum_i \sigma_i + \frac{\delta^2 L^2}{2} \right] \left(\sum_{n=1}^{m} k_n z_n \eta_n^2 \right) + \sum_{n=1}^{m} (k_n \eta_n^2 \delta^2) \sum_{\langle i,j \rangle_n} \sigma_i \sigma_j + pL^3 c x^2,$$

where z_n is the coordination number of the nth nearest neighbour, L is the number of sites in each direction, and c is the unit cell parameter. Because the c axis length responds to the spin states of the Fe atoms in a complicated way, we make the simplifying assumption that it is constant and set $c = 15.2$ Å. Minimising over x yields

$$x_{min} = \left[\frac{(\sum_{n=1}^{m} k_n z_n \eta_n^2)}{(\sum_{n=1}^{m} k_n z_n \eta_n^2) + 4pL\ell} \right] \left(\bar{R} + \frac{2\delta}{N_s} \sum_i \sigma_i \right)$$

Substituting x_{min} into the Hamiltonian, and neglecting constant terms, we arrive at an Ising-Husimi-Temperley model

$$H = \sum_{n=1}^{m} J_n \sum_{\langle i,j \rangle_n} \sigma_i \sigma_j - \frac{J_\infty(p)}{N_s} \sum_{i,j} \sigma_i \sigma_j + h_{\text{eff}}(p) \sum_i \sigma_i,$$

where $J_n = k_n \eta_n^2 \delta^2$, $J_\infty(p) = \frac{(\sum_m J_m)^2 \delta^2}{(\sum_m J_m) + 4p}$ is a long-range strain interaction that couples every spin to every other spin and $h_{eff}(p) = \left(\frac{4(\sum_m J_m)\, p\bar{R}\delta}{(\sum_m J_m) + 4p} + \frac{1}{2}\Delta G \right)$ is an effective field.

We solve this model in 2D (or equivalently assume identical layers) via Monte Carlo simulations on a 3600-site lattice (i.e., $L = 60$) with periodic boundary conditions. We employ heating and cooling simulations allowing single pseudospin flip moves, and parallel tempering between simulations. For each point we perform 1500 measurements after equilibrating for 36,000 Monte Carlo moves with 3600 Monte Carlo moves between each point. In the equilibration phase of the parallel tempering run we use both single pseudospin flip and parallel tempering move to find the lowest free energy state.

S2. Thermogravimetric analysis (TGA)

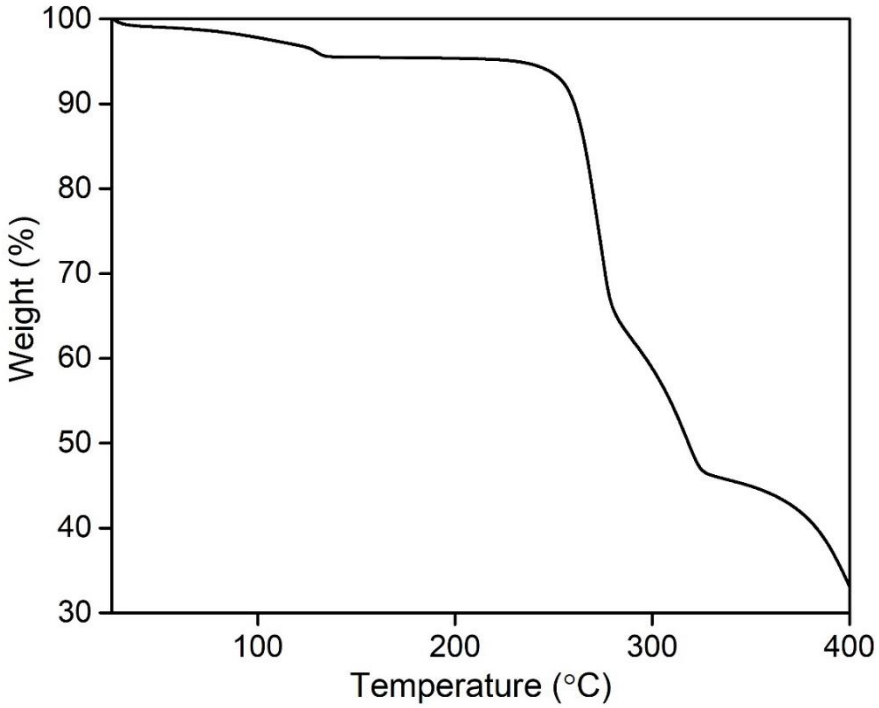

Figure S1. Thermogravimetric analysis data for **A**·3H_2O (water loss experimental 7.05% *cf*. calculated 7.45%).

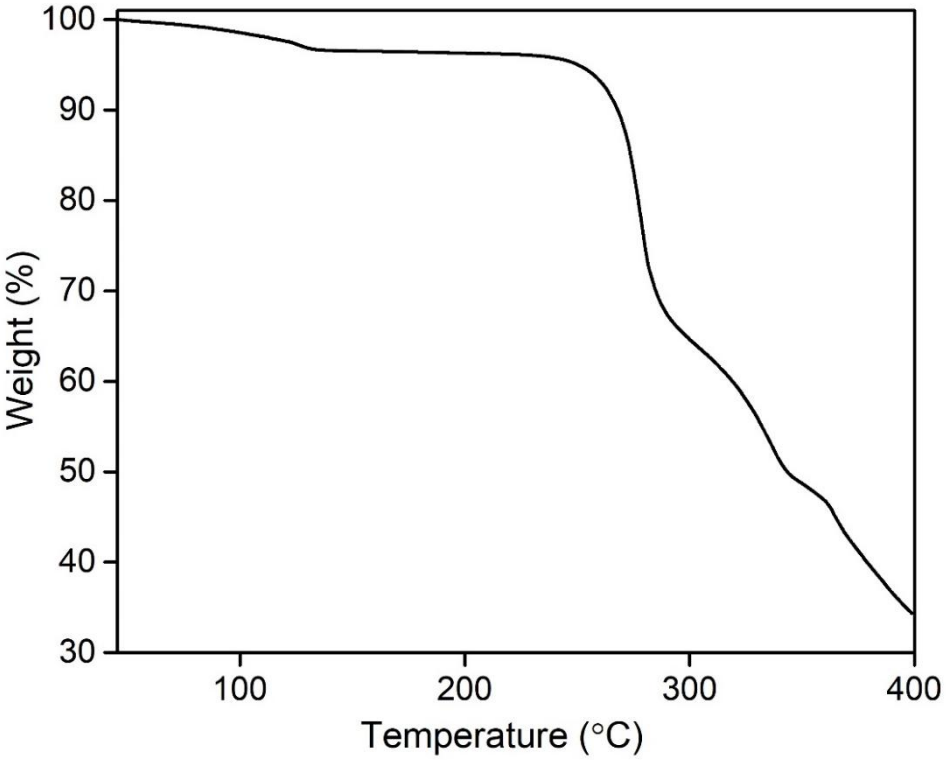

Figure S2. Thermogravimetric analysis data for **A**·2H_2O (water loss experimental 4.98% *cf*. calculated 5.15%).

S3. Differential scanning calorimetry (DSC)

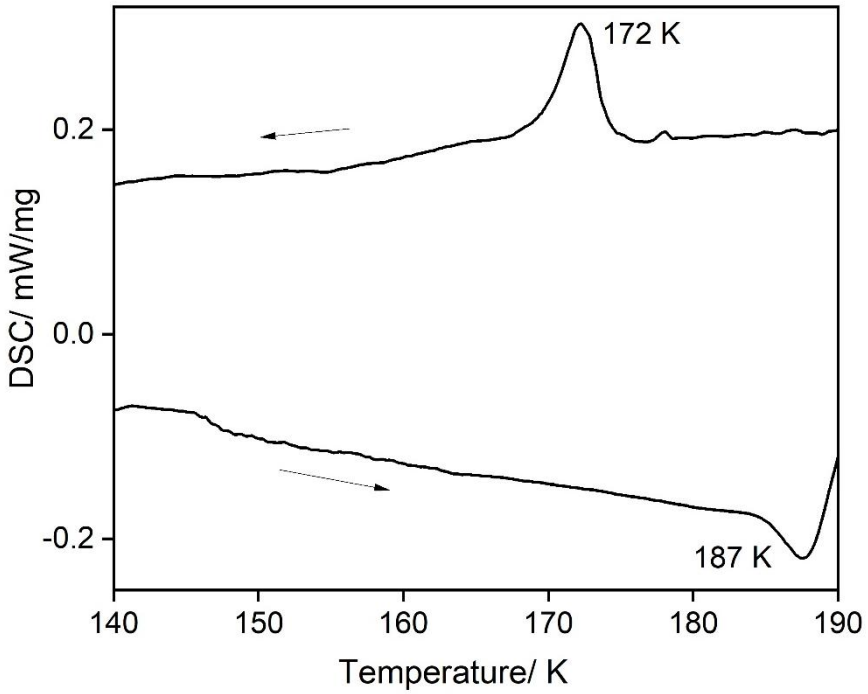

Figure S3. Differential scanning calorimetry data for **A**·3H_2O.

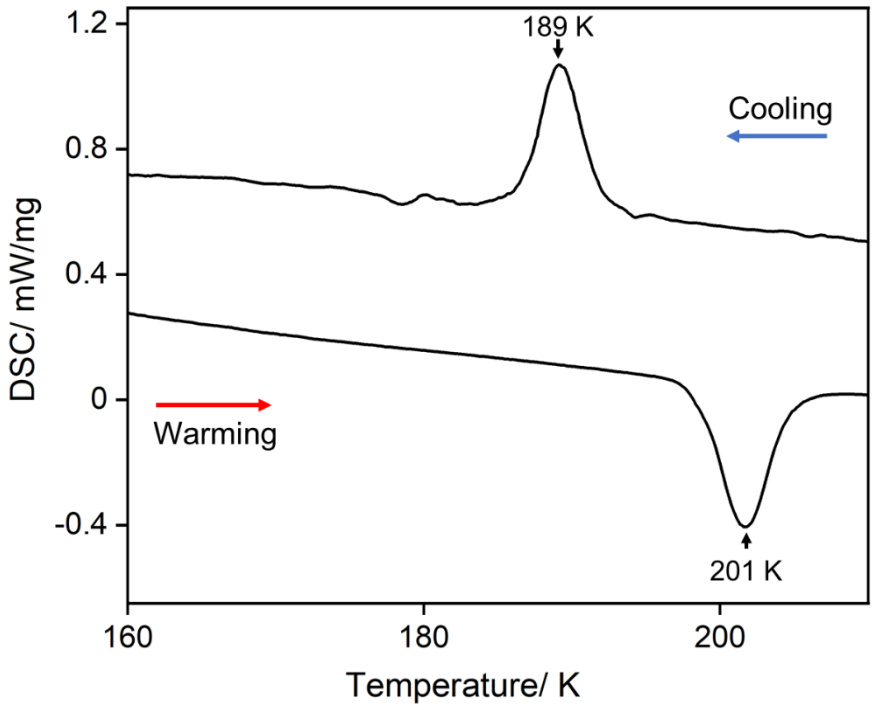

Figure S4. Differential scanning calorimetry data for **A**·2H_2O.

S4. Powder X-ray diffraction

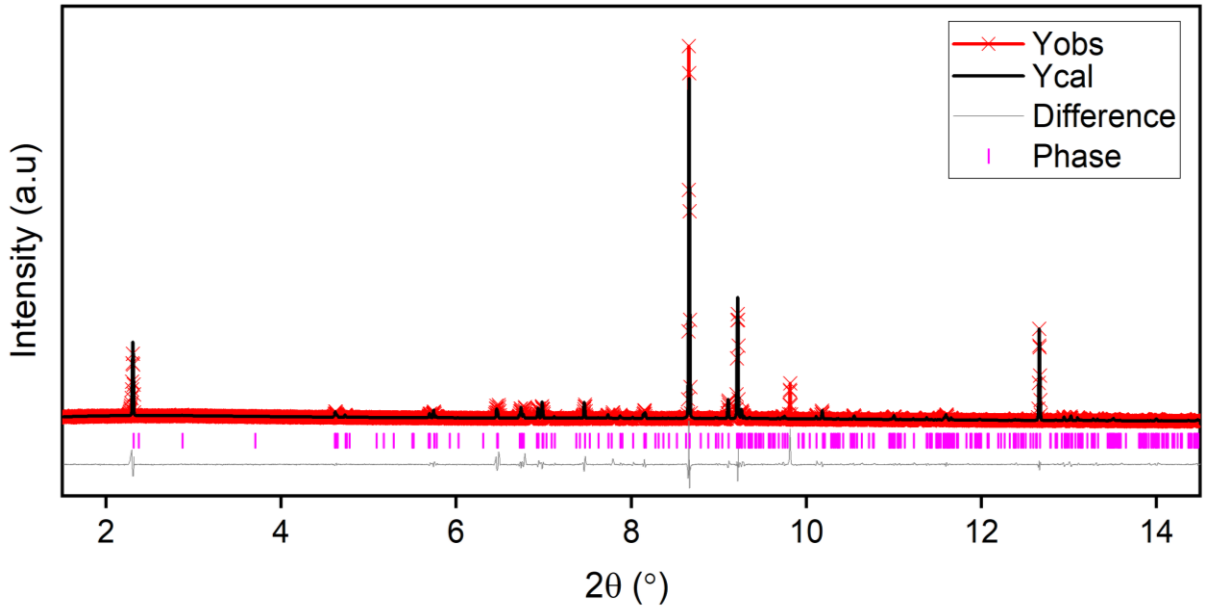

Figure S5. Le Bail refinement for **A**·3H_2O at 210 K. Refined parameters: *a* = 7.451 Å, *b* = 14.712 Å and *c* = 15.327 Å, *α* = 104.157°, *β* = 99.838°, *γ* = 90.109°, V = 1603.7 Å^3 (*cf*. single crystal at 210 K: *a* = 7.442, *b* = 14.704, *c* = 15.329, *α* = 104.199°, *β* = 99.924°, *γ* = 90.316°, V = 1599.90 Å^3).

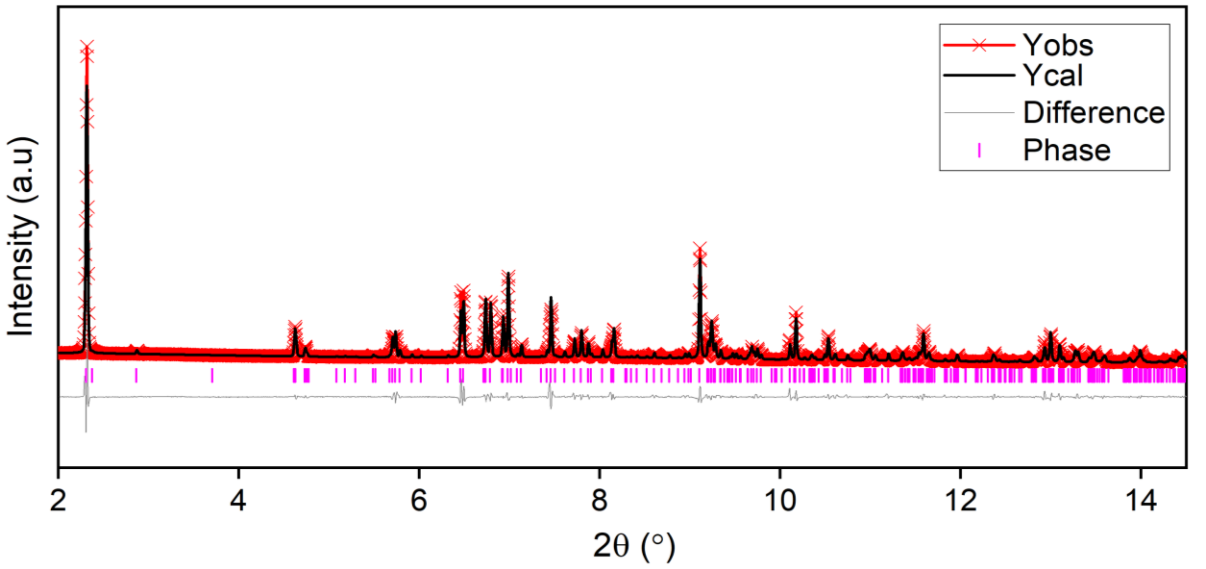

Figure S6. Le Bail refinement for **A**·2H_2O at 250 K. Refined parameters: *a* = 7.458 Å, *b* = 14.719 Å and *c* = 15.375 Å, *α* = 104.303°, *β* = 99.864°, *γ* = 90.310°, V = 1609.4 Å^3 (*cf*. single crystal at 250 K: *a* = 7.442, *b* = 14.716, *c* = 15.327, *α* = 104.126°, *β* = 99.888°, *γ* = 90.254°, V = 1601.8 Å^3).

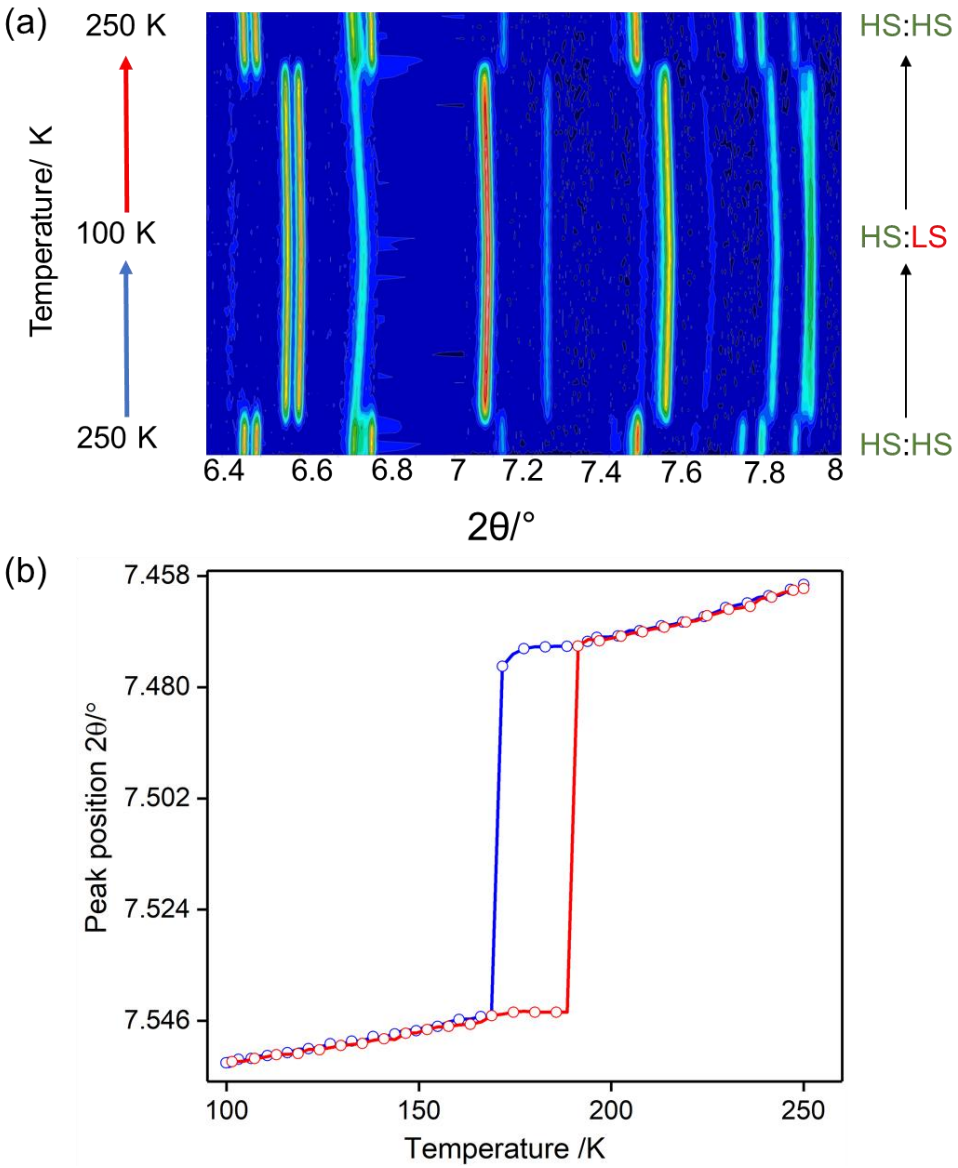

Figure S7. Variable temperature powder X-ray diffraction data for **A**·3H_2O (250 – 100 – 250 K). Showing (a) the qualitative shift in Bragg peaks over the region 6.4 – 8 °and (b) the qualitative shift in the reflection 0 3 -2; the temperature and character of peak shift matches well with magnetic susceptibility data.

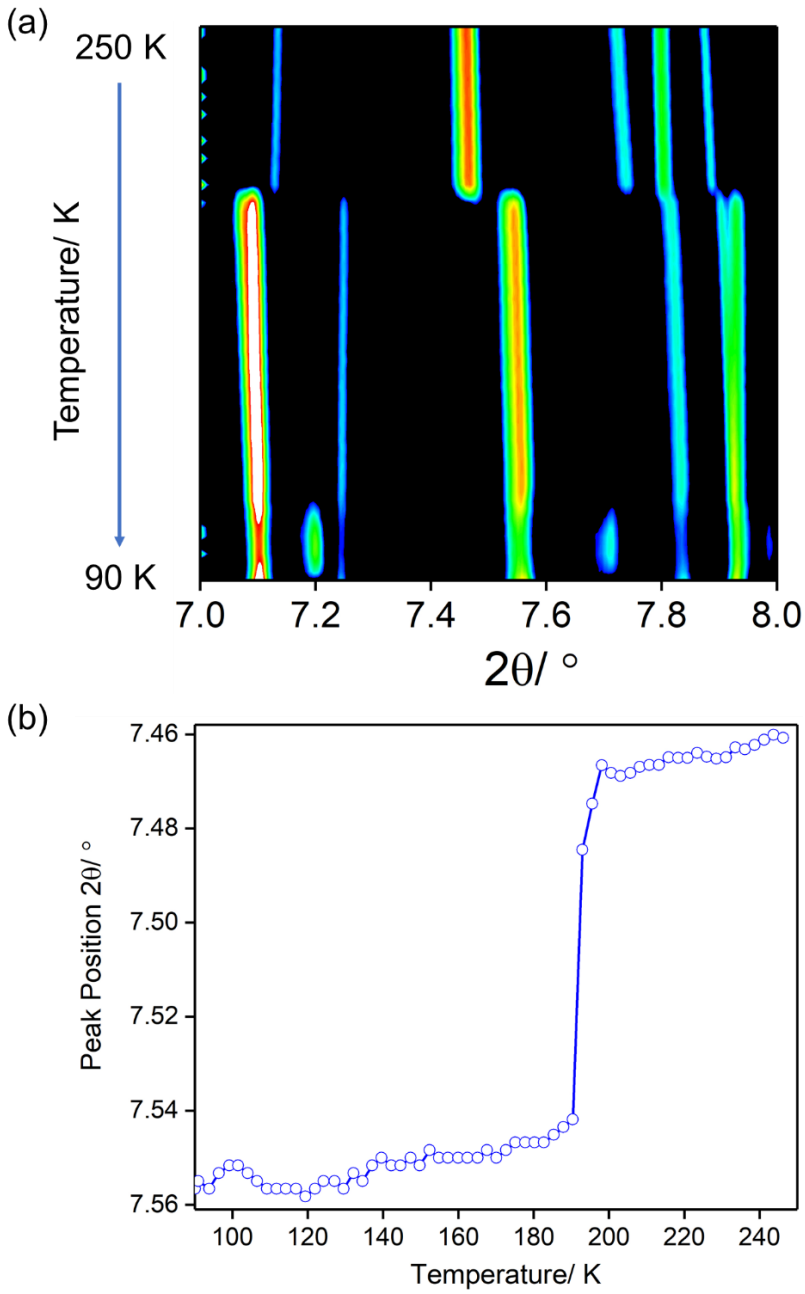

Figure S8. Variable temperature powder X-ray diffraction data for **A**·2H_2O (250 – 90 K). Showing (a) the qualitative shift in Bragg peaks over the region 7.0 – 8.0 °and (b) the qualitative shift in the reflection 0 3 -2. Note that the lower temperature SCO step could not be monitored due to the cryostream limit being 90 K. Also, only data on cooling was able to be obtained owing to limitations on synchrotron beamtime. The temperature and character of the peak shift associated with the higher temperature hysteresis loop matches well with magnetic susceptibility data.

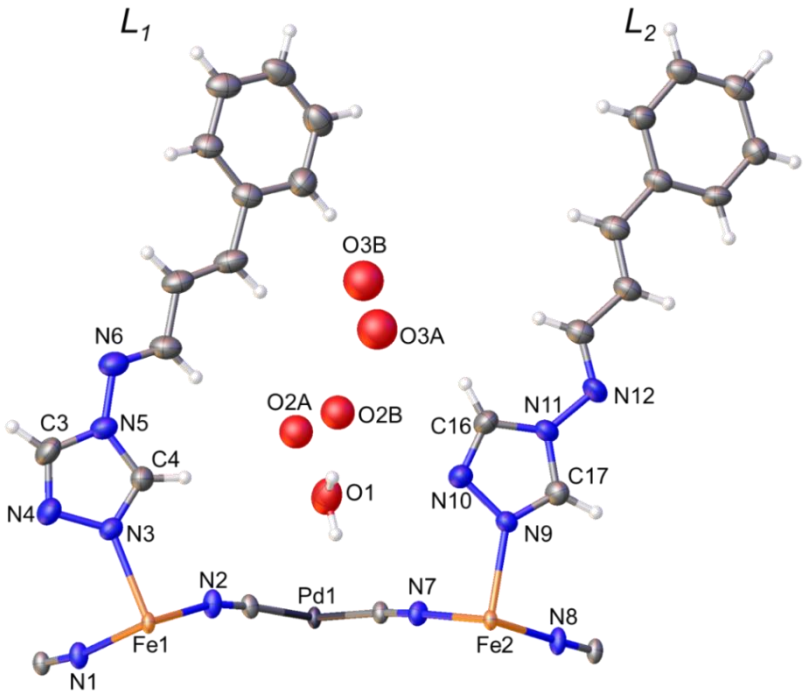

S5. Single crystal X-ray diffraction

Figure S9. Asymmetric unit of **A**·3H_2O at 210 K, disordered water molecules shown (O2A/B and O3A/B).

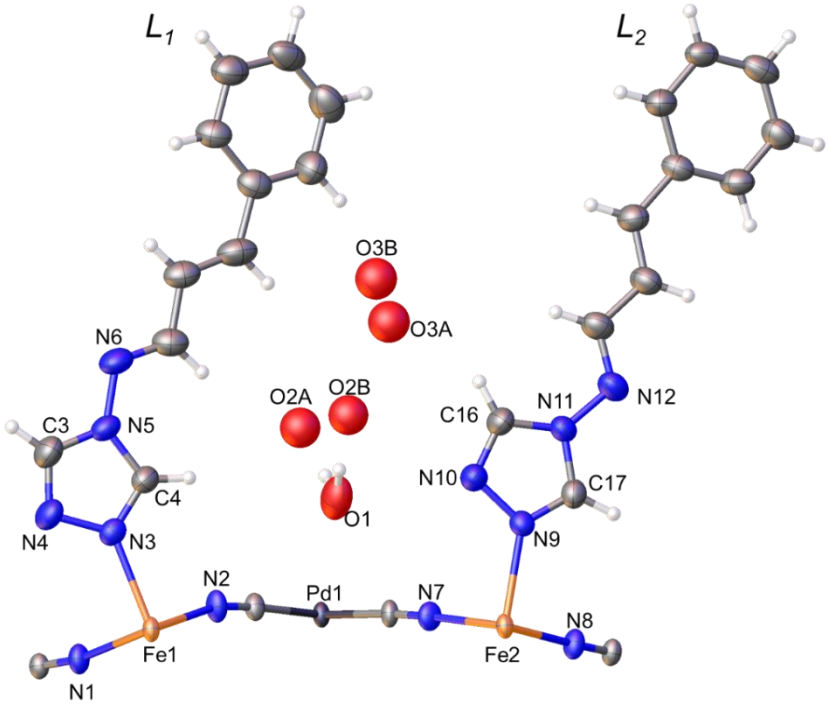

Figure S10. Asymmetric unit of **A**·2H_2O at 250 K, disordered water molecules shown (O2A/B and O3A/B).

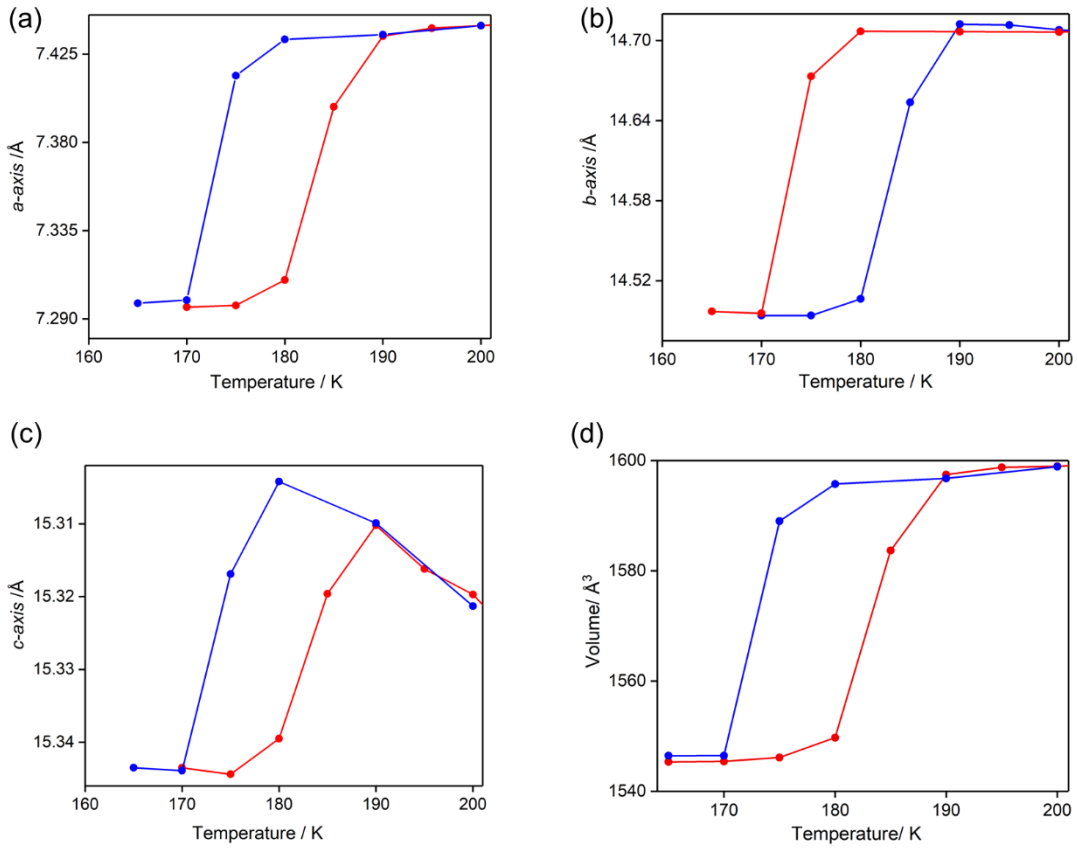

Figure S11. Variable temperature single crystal X-ray diffraction data for **A**·3H_2O (200 – 165 – 200 K) showing the (a) *a*-axis, (b) *b*-axis, (c) *c*-axis and (d) unit cell volume. The overall volume change is 3.5% which is consistent with a 50% SCO transition.

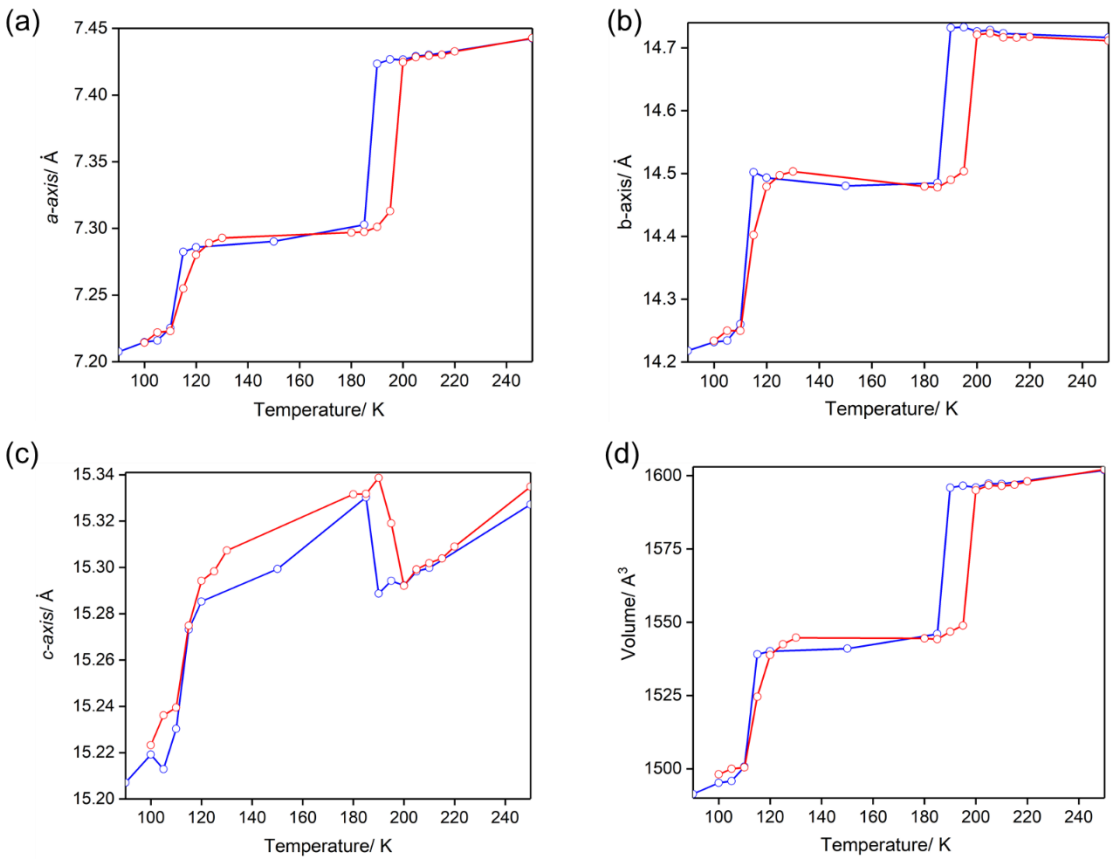

Figure S12. Variable temperature single crystal X-ray diffraction data for **A**·2H_2O (250 – 90 – 250 K) showing the (a) *a*-axis, (b) *b*-axis, (c) *c*-axis and (d) unit cell volume. The overall volume change is 7.3% which is consistent with a complete SCO transition.

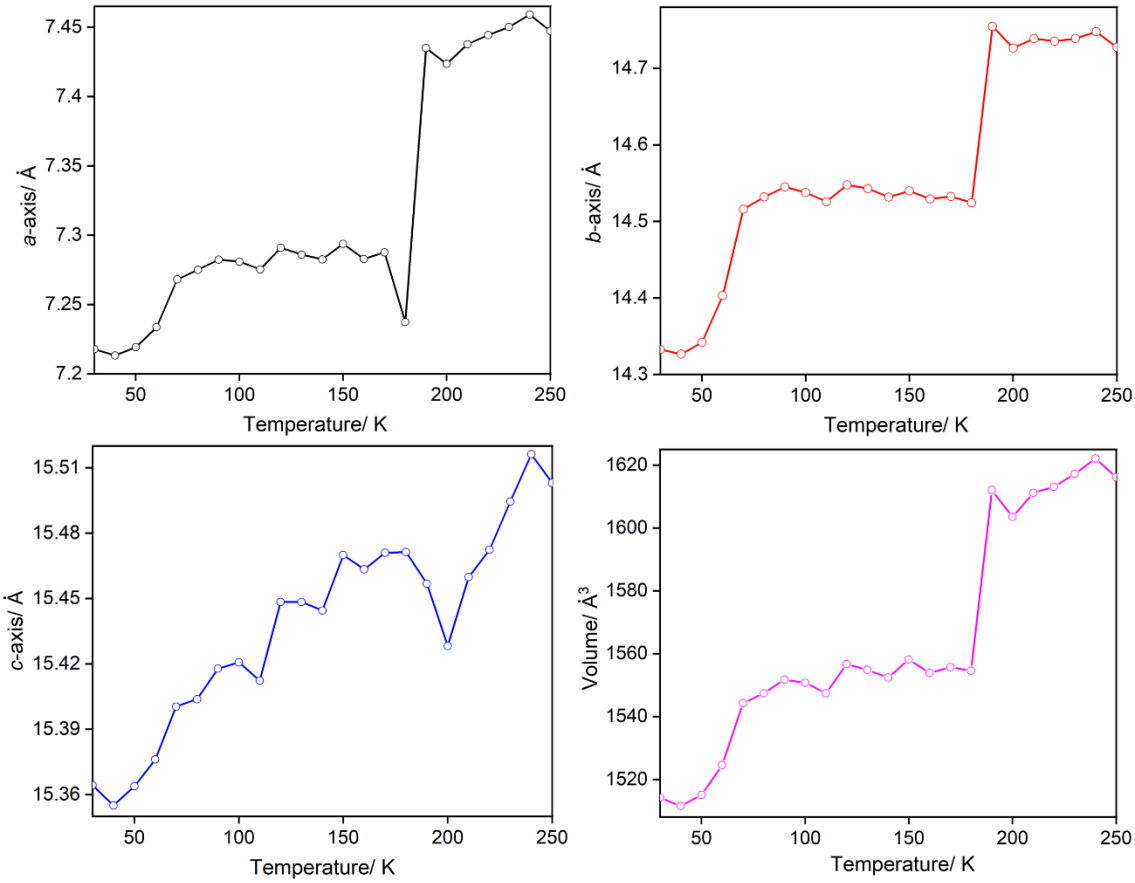

Figure S13. Single crystal unit cell parameter (*a*, *b* and *c*) and cell volume of **A**·3H_2O upon heating (30 – 250 K) in the absence of red-light irradiation.

Table S1. Single crystal data and refinement details for **A**·3H_2O representative of the HS-HS and HS-LS states and **A**·2H_2O representative of the HS-HS, HS-LS and LS-LS states (Fe1-Fe2).

	A·3H_2O		**A**·2H_2O		
Formula/ FW	**$C_{26}H_{22}PdFeN_{12}O_3$/712.80**		**$C_{26}H_{20}PdFeN_{12}O_2$/694.80**		
Temperature/K	210	170	250	150	90
Symmetry	Triclinic ($P\bar{1}$)		Triclinic ($P\bar{1}$)		
***a* / Å**	7.4421(3)	7.2960(3)	7.4424(2)	7.2887(3)	7.2076(2)
***b* / Å**	14.7043(5)	14.4939(5)	14.7164(4)	14.4913(5)	14.2180(6)
***c* / Å**	15.3292(6)	15.3385(7)	15.3272(5)	15.2974(7)	15.2071(8)
α / °	104.199(3)	104.396(4)	104.126(3)	104.202(4)	103.633(4)
β / °	99.924(3)	99.938(4)	99.888(3)	99.926(4)	99.691(3)
γ / °	90.316(3)	90.366(3)	90.254(2)	90.313(3)	90.142(3)
Volume / $Å^3$	1599.90(11)	1545.44(11)	1601.88(8)	1540.99(11)	1491.42(11)
ρ_{calc}mg / mm^3	1.480	1.532	1.457	1.654	1.520
Data/restraints/parameters	10327/0/401	9987/0/400	10443/0/401	10041/0/387	9666/0/377
Goodness–of–fit on F^2	1.040	1.070	1.055	1.102	1.040
Final R indexes [I>=2σ (I)] [a], [b]	0.0687,0.1006	0.0819,0.1120	0.0893,0.1144	0.1085,0.1311	0.1070,0.1370
Final R indexes [all data] [a], [b]	0.1935,0.2089	0.2137,0.2271	0.2394,0.2550	0.2842,0.2970	0.2831,0.3025

[a] $R_1 = \Sigma||F_o| - |Fc||/\Sigma|F_o|$. [b] $wR_2 = [\Sigma w(F_o^2 - F_c^2)_2/\Sigma w(F_o^2)^2]^{½}$.

Table S2. Selected structural parameters from variable temperature single crystal data for **A**·3H_2O representative of the HS-HS and HS-LS states and **A**·2H_2O representative of the HS-HS, HS-LS and LS-LS states (Fe1-Fe2).

	A·3H_2O		**A**·2H_2O		
Temperature /K	210	170	250	150	90
$<d_{Fe1-N}>$ /Å[a]	2.165	2.155	2.162	2.154	1.964
$<d_{Fe2-N}>$ /Å[a]	2.150	1.961	2.156	1.958	1.955
Σ_{Fe1} /°[b]	5.44	13.64	5.84	14.4	11.2
Σ_{Fe2} /°[b]	14.4	6.0	11.16	4.8	7.6
Ligand twist (L_1, L_2)	10.3, 14.6	11.1, 12.3	10.9, 15.3	12.3, 12.8	11.5, 15.5
Fe-N-N^{trz} bite angle (L_1, L_2)	123.48, 125.33	122.12, 124.75	123.03, 125.66	121.38, 124.71	122.08, 122.27
V_{Oh} Fe1/ Å^3	13.37	13.02	13.32	13.09	10.00
V_{Oh} Fe2/ Å^3	14.17	10.48	14.11	10.33	10.49
host (H)-host (H) interactions /Å					
N12…C3	3.329(9)	3.293(11)	3.335(12)	3.291(13)	3.305(14)
host (H)-guest (G) interactions /Å					
N10···O1	2.911(8)	2.850(8)	2.892(9)	2.847(10)	2.838(11)
guest (G)-guest (G) interactions /Å					
O1···O2A/B	2.74(11)/2.86(13)	2.77(11)/2.84(15)	2.74(15)/2.85(18)	2.77(13)/2.86(15)	2.77(10)/2.86(12)
Aromatic (L_1···L_2)	3.682(4),3.888(4)	3.548(5),3.520(5)	3.595(4),3.618(5)	3.495(5),3.624(5)	3.442(5),3.589(5)

Table S2 continued. Selected structural parameters from variable temperature single crystal data for **A**·3H_2O representative of the HS-HS and HS-LS states and **A**·2H_2O representative of the HS-HS, HS-LS and LS-LS states (Fe1-Fe2).

	A·3H_2O		**A**·2H_2O		
Temperature /K	210	170	250	150	90
ϑ**1 /°** [c]	88.9(16)	88.1(2)	89.22(18)	87.90(3)	89.7(3)
ϑ**2 /°** [d]	89.1(18)	90.1(2)	89.20(2)	90.20(3)	89.8(3)
$\Sigma_{\varphi 1+\varphi 2+\varphi 3}$ **/°** [e]	38.5	36.1	38.2	36.8	33.6

Inter-layer /Å [f]	15.288(7)	15.248(8)	15.297(6)	15.235(8)	15.193(9)
<H-N> /Å [g]	3.147	3.043	3.141	3.040	2.989

[a] average Fe-N distance; [b] sum of the difference of the 12 *cis* N-Fe-N angles from 90 °; [c] ∠N1-Fe1-N2; [d] ∠N7-Fe2-N8
[e] Sum of the angles between the planes defining the three symmetry-independent $(Fe^{II}_2[Pd^{IV}(CN)_4]_2)_n$ grids
[f] distance between Fe1 and Fe2 on adjacent layers; [g] average H-N distance between cintrz C-H and N of cyano bridge in adjacent layer (H4-N2, H3-N1, H16-N7, H17-N8).

Table S3. Single crystal data and refinement details for **A**·3H_2O under light irradiation.

Temperature/K	**30**	**30**
Light source	dark	red
Crystal system	Triclinic	Triclinic
Space group	$P\bar{1}$	$P\bar{1}$
***a* / Å**	7.2893(3)	7.2166(4)
***b* / Å**	14.5531(7)	14.3326(7)
***c* / Å**	15.4588(6)	15.3607(8)
α / °	104.945(4)	104.500(5)
β / °	100.108(4)	99.873(4)
γ / °	90.354(4)	90.217(4)
Volume / Å^3	1557.55(13)	1513.59(14)
ρ_{calc}mg / mm^3	1.533	1.454
Data/restraints/parameters	6171/0/365	5939/0/360
Goodness–of–fit on F^2	1.165	1.095
Final R indexes [I>=2σ (I)][a], [b]	0.0565,0.1384	0.0671,0.1597
Final R indexes [all data] [a], [b]	0.0839,0.1650	0.1026,0.1969

[a] $R_1 = \Sigma||F_o| - |Fc||/\Sigma|F_o|$. [b] $wR_2 = [\Sigma w(F_o^2 - F_c^2)_2/\Sigma w(F_o^2)^2]^{½}$.

Table S4. Selected structural parameters for the reverse-LIESST structure of **A**·3H_2O.

Temperature/K	**30**	**30**
Light source	dark	red
$<d_{Fe1-N}>$ /Å[a]	2.163(5)	2.00(6)
$<d_{Fe2-N}>$ /Å[a]	1.960(5)	1.969(6)
Σ_{Fe1} /°[b]	12.01	11.60
Σ_{Fe2} /°[b]	8.40	5.60
Fe-N-N^{trz} bite angle (L_1, L_2)	90.2, 88.9	91.3, 89.2
ϑ1 (°) [c]	87.8(2)	89.5(3)
ϑ2 (°) [d]	90.5(2)	89.8(3)
$\Sigma_{\varphi 1+\varphi 2+\varphi 3}$ (°) [e]	37.08	34.58
Inter-layer (Å) [f]	15.711	15.237
V_{Oh} Fe1/ Å^3	13.55	10.61
V_{Oh} Fe2/ Å^3	10.03	9.99
Aromatic (L_1···L_2)	3.729(4), 3.891(4)	3.591(5), 3.883(5)

[a] average Fe-N distance, [b] sum of the difference of the 12 cis N-Fe-N angles from 90 °, [c] ∠N1-Fe1-N2; [d] ∠N7-Fe2-N8, [e] Sum of the angles between the planes defining the three symmetry-independent $(Fe^{II}_2[Pd^{IV}(CN)_4]_2)_n$ grids, [f] Fe…Fe distance between the neighbouring layers.

Table S5. Unit cell dimensions of **A**·3H_2O during compression of a single crystal in a pressure-transmitting medium of MiTeGen LVCO-5 Cryo Oil™. The crystals retain $P\bar{1}$ symmetry. Data are collected at T = 295 K. The dashed lines mark the HS-HS to HS-LS to LS-LS transitions and piezochromism from yellow to orange to red.

P **(GPa)**	***a*** **(Å)**	***b*** **(Å)**	***c*** **(Å)**	***α*** **(°)**	***β*** **(°)**	***γ*** **(°)**	***V*** **(Å^3)**
0.00	7.4603 (10)	14.7235 (2)	15.3847 (2)	104.156 (10)	99.934 (10)	90.291 (10)	1612.02 (4)
0.14	7.4531 (4)	14.7034 (14)	15.3370 (14)	104.075 (8)	99.959 (6)	90.300 (7)	1603.7 (2)
0.36	7.4411 (4)	14.6877 (14)	15.2752 (15)	103.938 (8)	99.965 (7)	90.292 (7)	1593.9 (2)
0.57	7.2123 (4)	14.2972 (15)	15.0613 (15)	103.393 (9)	100.253 (7)	90.318 (8)	1484.9 (2)
1.01	7.1408 (4)	14.0263 (14)	14.8270 (14)	102.690 (8)	100.087 (7)	90.167 (7)	1425.1 (2)
1.72	7.1336 (3)	13.8800 (13)	14.6354 (13)	102.050 (8)	100.151 (5)	90.106 (5)	1393.9 (2)
2.75	7.144 (4)	13.686 (8)	14.551 (6)	100.66 (4)	102.38 (6)	90.35 (7)	1364.0 (13)

Table S6. Structural parameters for **A**·3H_2O during compression in a pressure-transmitting medium of MiTeGen LVCO-5 Cryo Oil™. Data are collected at *T* =

***P* (GPa)**	**Fe1-N /Å**	**Fe2-N /Å**	**Σ^{Fe1} /°**	**Σ^{Fe2} /°**	**V_{Oh}^{Fe1} /Å^3**	**V_{Oh}^{Fe2} /Å^3**	**ϑ1 /° [a]**	**ϑ2 /°[b]**	**$\Sigma_{\varphi 1+\varphi 2+\varphi 3}$ /°[c]**	**Inter-layer /Å [d]**	**<H-N> /Å [e]**	**< π-π> (Å) [f]**
0.00	2.170(2)	2.162(2)	4.2	13.35	13.64	13.30	89.05(8)	89.22(8)	38.04	15.345(2)	2.958	3.875(19)

295 K. The dashed lines mark the HS-HS to HS-LS to LS-LS transitions and piezochromism from yellow to orange to red.

0.14	2.183(3)	2.158(3)	20.0	5.20	14.18	13.51	87.3(8)	89.7(9)	36.80	15.311(16)	2.950	3.866(11)
0.36	2.165(2)	2.134(2)	16.0	12.8	13.24	13.11	88.2(8)	89.1(9)	38.20	15.271(17)	2.945	3.859(12)
0.57	2.058(3)	1.959(3)	16.8	12.8	11.62	9.91	87.4(2)	87.9(10)	36.46	15.101(17)	2.810	3.790(11)
1.01	1.953(3)	1.901(2)	18.8	20.3	10.91	9.38	90.7(14)	93.7(15)	35.88	14.944(16)	2.840	3.608(15)
1.72	1.951(2)	1.906(2)	20.0	28.1	10.35	9.59	91.8(13)	95.9(15)	40.82	14.831(15)	2.845	3.582(15)

[a] ∠N1-Fe1-N2; [b] ∠N7-Fe2-N8.
[c] Sum of the angles between the planes defining the three symmetry-independent $(Fe^{II}_2[Pd^{IV}(CN)_4]_2)_n$ grids.
[d] Fe…Fe distance between neighbouring layers; [e]average H-N distance between cintrz C-H and N of cyano bridge in adjacent layer (H4-N2, H3-N1, H16-N7, H17-N8).
[f] average π-π distance between pairs of interacting cintrz ligand on adjacent layers.

Table S7. Changes to the unit cell volume, bulk modulus, and linear compressibility of **A**·3H_2O during compression.

Medium	***Max. P* (GPa)**	**Δ*V* (Å^3)**	**HS to LS (GPa)**	**Δ*V* (HS to LS) (Å^3)**
Cryo Oil	2.75	-248 (-15.4%)	0.36 to 0.57	-109 (-6.8%)
	K_0 (GPa)	**k_a (GPa^{-1})**	**k_b (GPa^{-1})**	**k_c(GPa^{-1})**
Cryo Oil	4.8 (5)	0.026	0.057	0.063

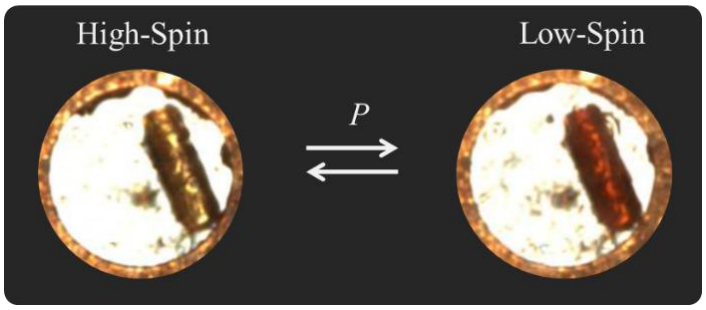

Figure S14. Reversible, piezochromic colour change in a single crystal of **A**·3H_2O from yellow (HS state, 0–0.36 GPa) to red (LS state > 0.57 GPa) upon hydrostatic compression.

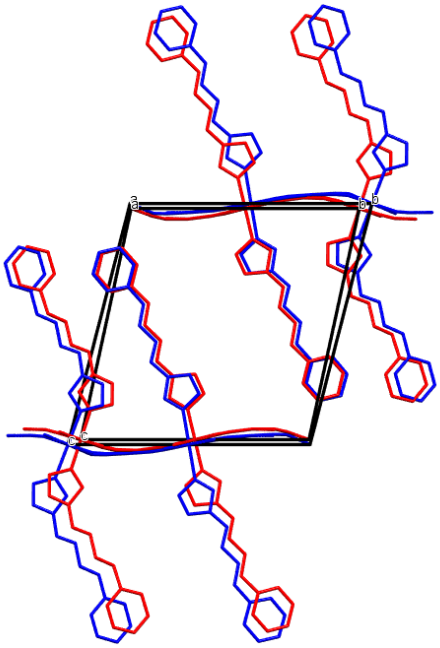

Figure S15. Structural overlay of **A**·3H_2O at ambient pressure (blue) and 1.72 GPa (red).

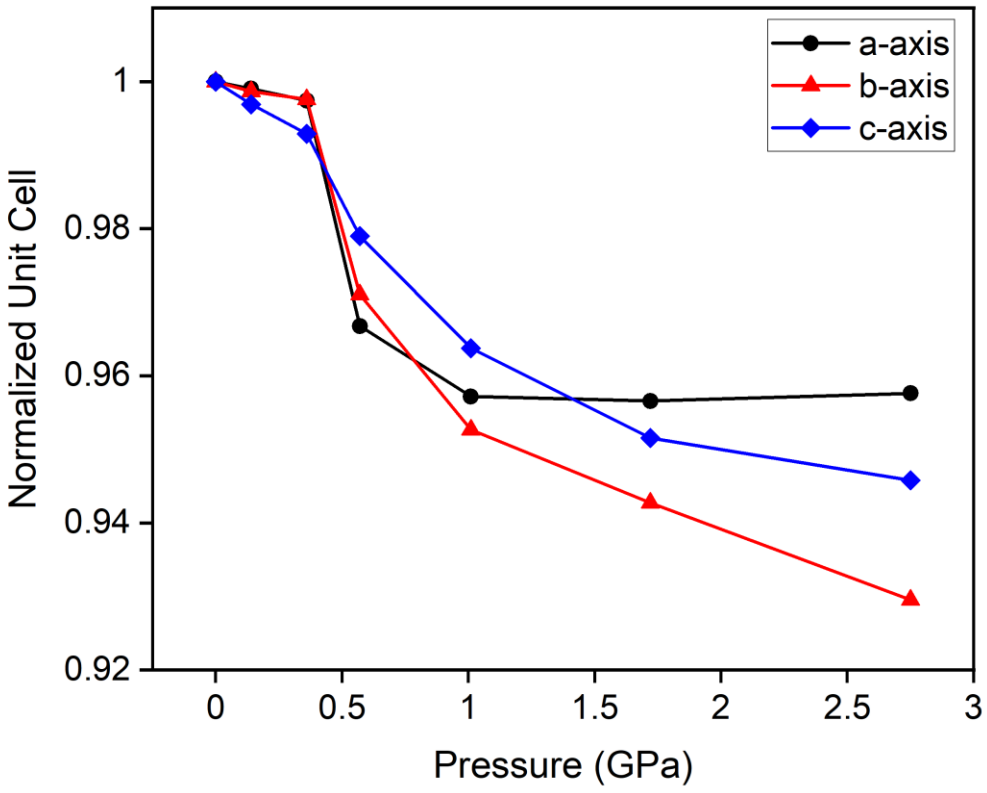

Figure S16. Unit cell axes of **A**·3H_2O during compression (0 – 2.75 GPa)

S6. Magnetic susceptibility

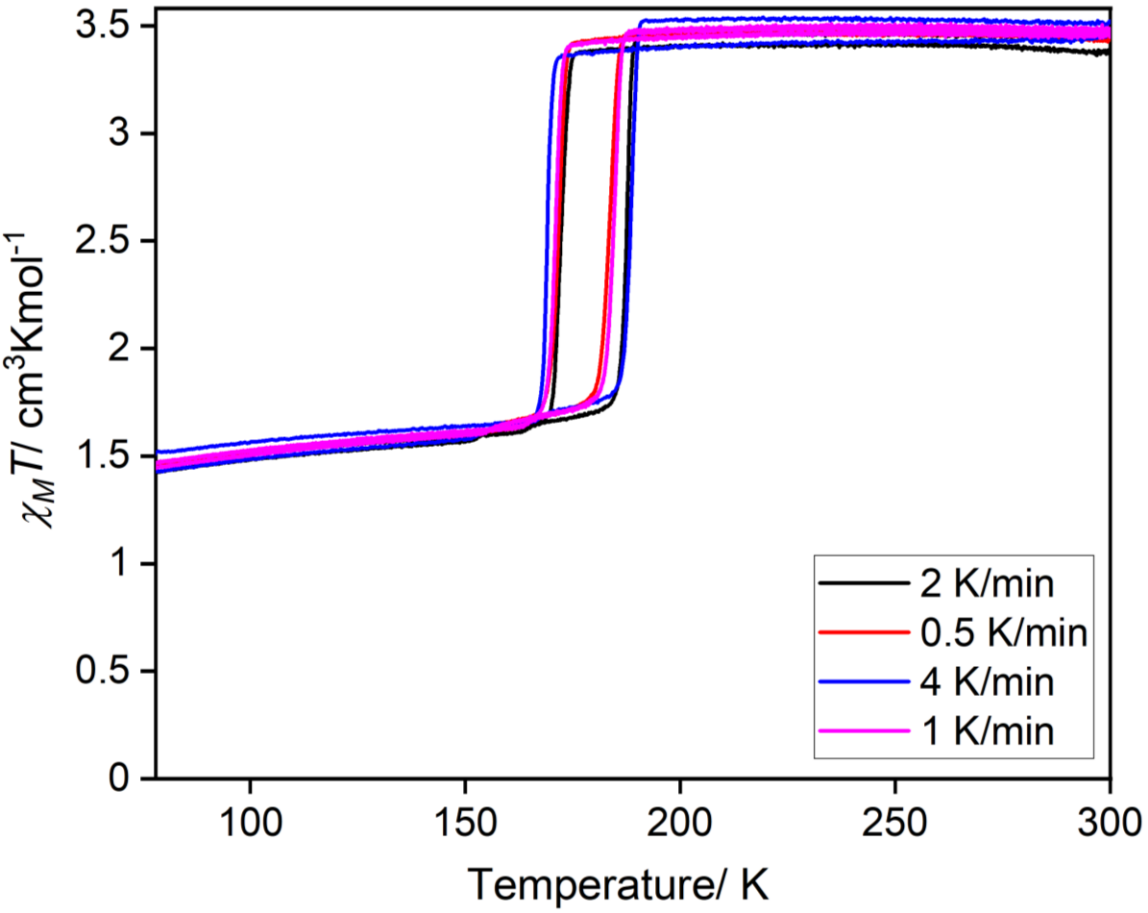

Figure S17. $\chi_M T$ versus T data for **A**·3H_2O collected in continuous mode at scan rates of 2, 0.5, 4 and 1 Kmin^{-1}, showing a contraction of the thermal hysteresis loop at slower scan rates.

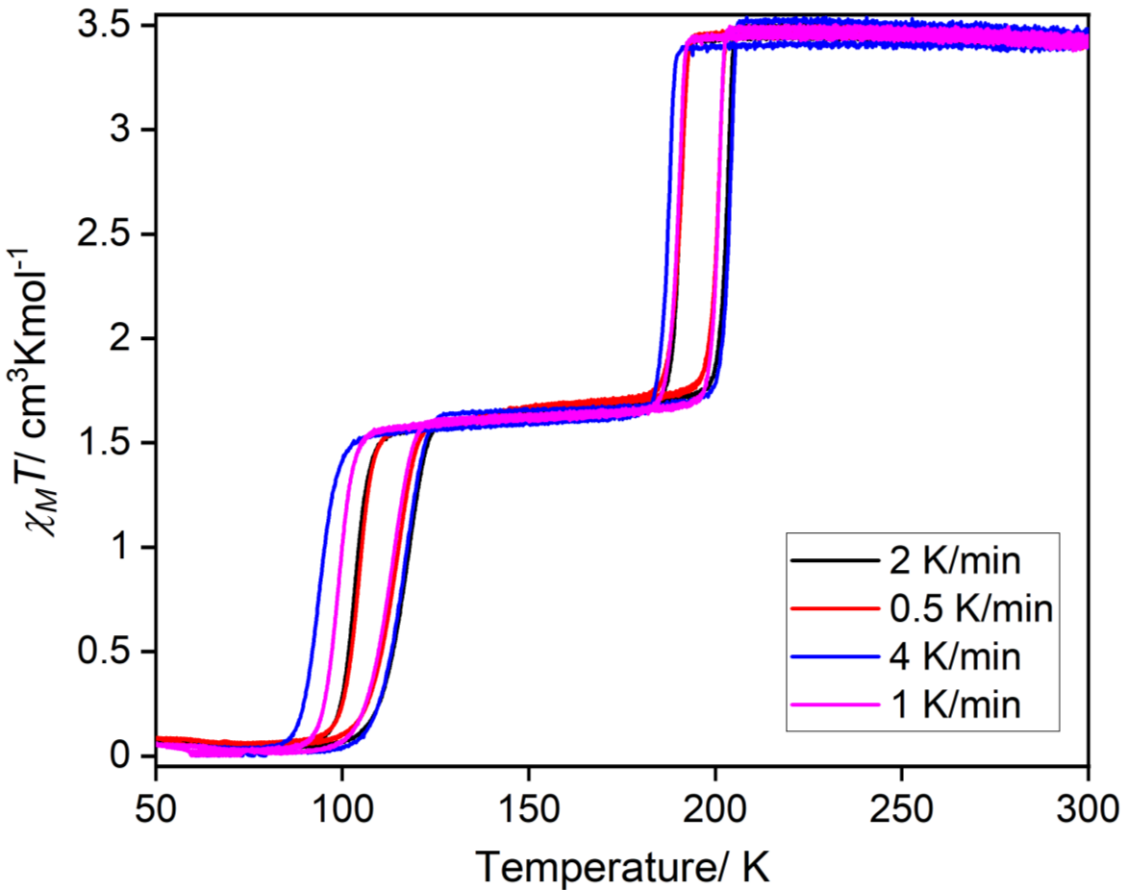

Figure S18. $\chi_M T$ versus T data for **A**·2H_2O collected in continuous mode at scan rates of 2, 0.5, 4 and 1 Kmin^{-1}, showing a contraction of the thermal hysteresis loop at slower scan rates.

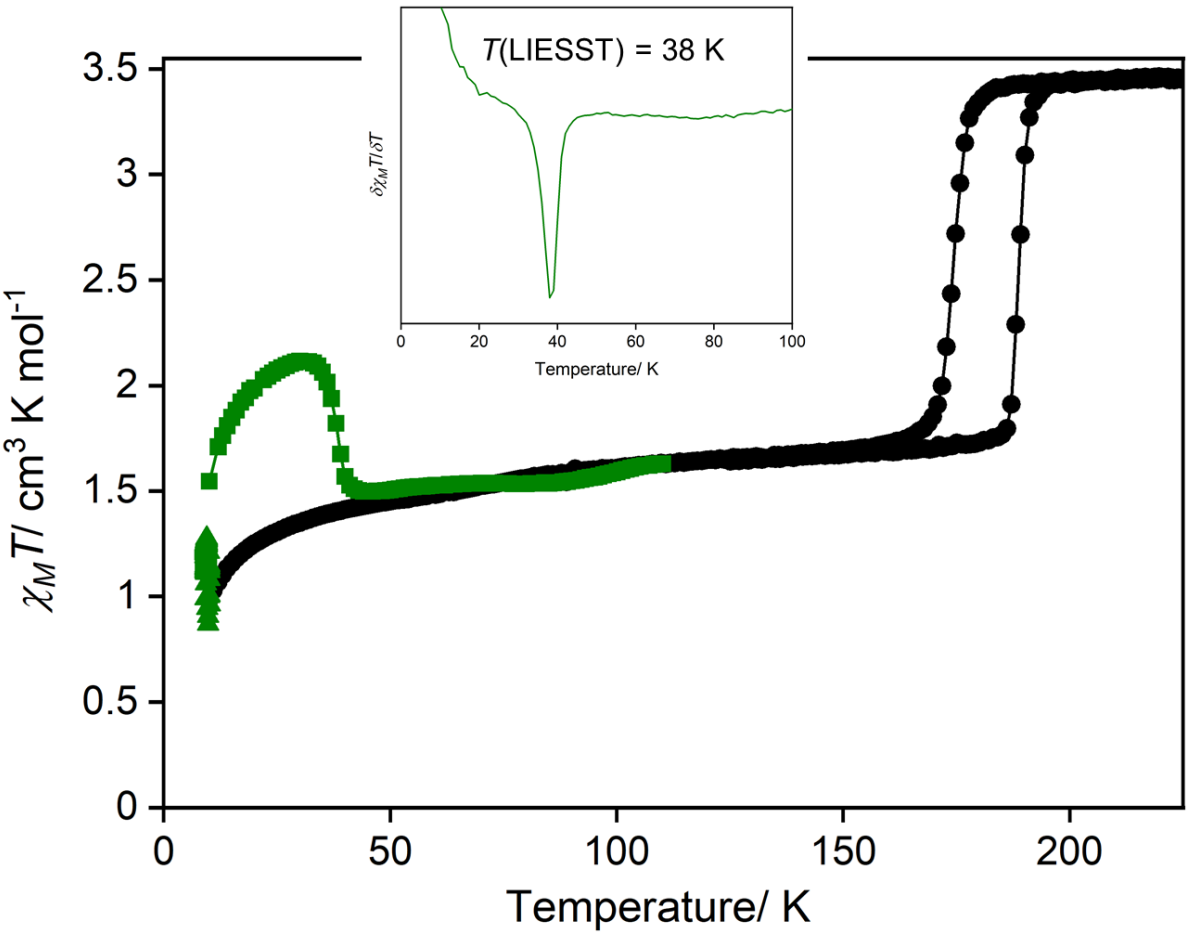

Figure S19. $\chi_M T$ versus T data for **A**·3H_2O showing the thermal SCO (•, 250 – 10 – 250 K), the photoexcitation at 10 K (green triangles, λ = 510 nm) and relaxation in the absence of light (10 – 100 K). Inset: $\delta_{\chi mT}/\delta T$ of the relaxation data showing a *T*(LIESST) of 38 K.

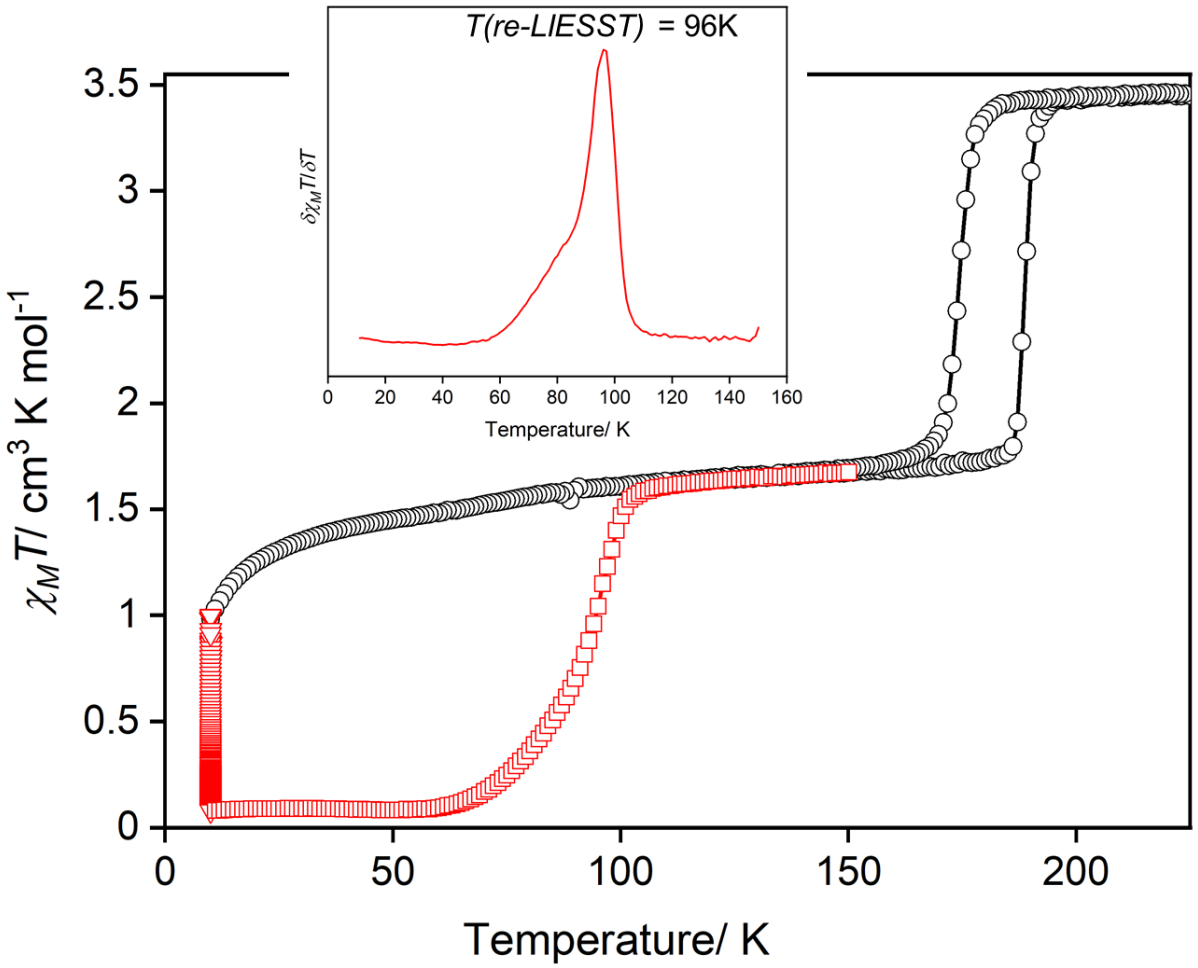

Figure S20. $\chi_M T$ versus T data for **A**·3H$_2$O showing thermal SCO (○, 150 – 250 – 10 K), the photoexcitation at 10 K (red triangles, λ = 830 nm) and relaxation in the absence of light (10 – 100 K). Inset: $\delta_{\chi mT}/\delta T$ of the relaxation data showing a T(re-LIESST) of 96 K (reverse LIESST).

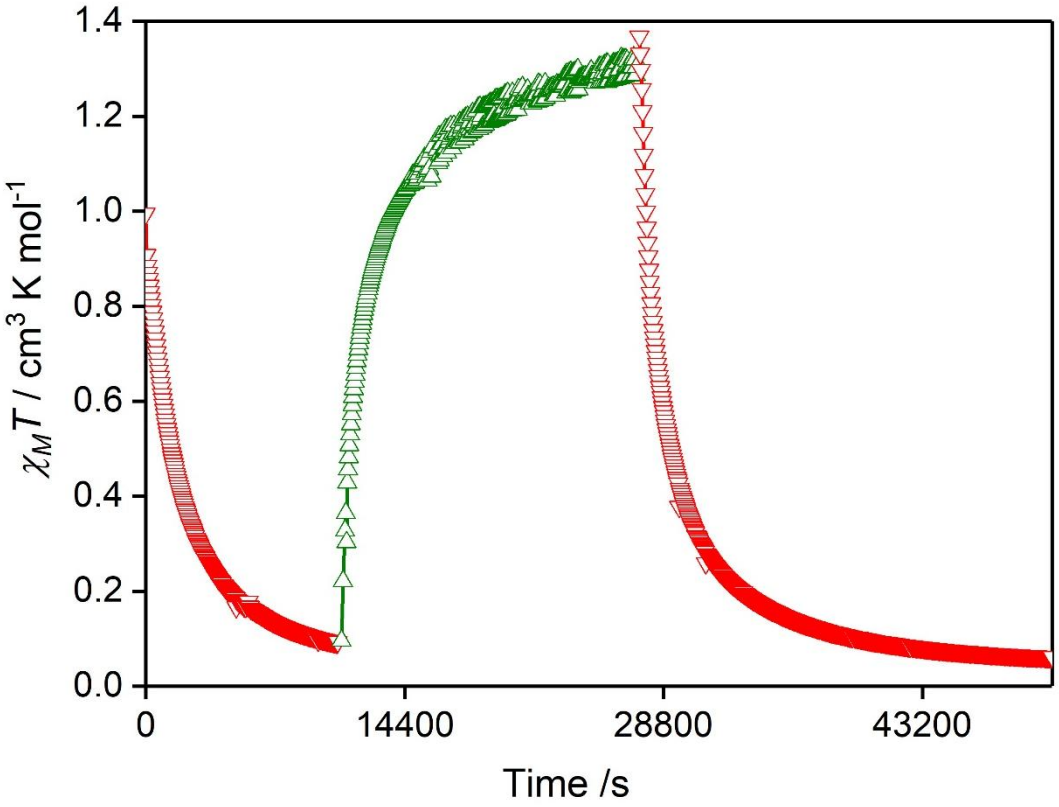

Figure S21. Photo-switching $\chi_M T$ values of **A**·3H_2O under irradiation of 510 nm (green) and 830 nm (red) at a constant temperature of 10 K.

S7. Elastic model

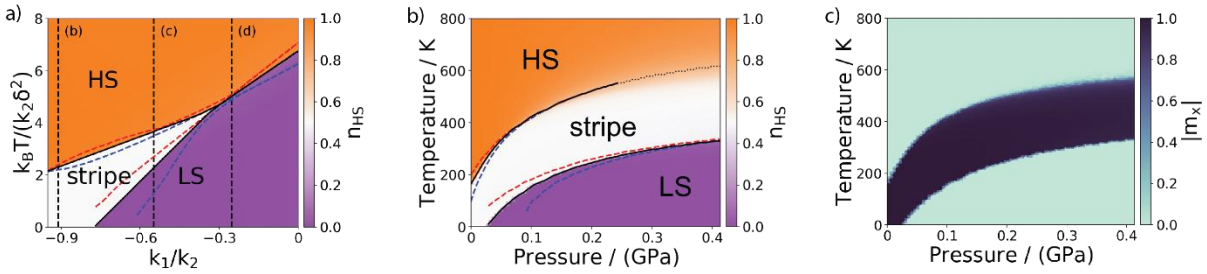

Figure S22. Finite temperature phase diagrams for (a) k_1/k_2, the relative strengths of the through -space and -bond interactions showing the heating, cooling and parallel tempering lines, (b) pressure showing the heating, cooling and parallel tempering lines and (c) the stripe order parameter with fixed $k_3 = k_1/2$, $k_4 = 0$, $k_5 = 0.1k_2$ and $\Delta H/k_2\delta^2 = 44\, k_1/k_2 + 43$. The shading in (a,b) indicates the fraction of high spins $n_{HS} \propto \chi T$, where χ is the magnetic susceptibility and (c) indicates the stripe order parameter $m_x = \sum_{i,j}(-1)^i \sigma_i \sigma_j$ calculated from parallel tempering. The solid black lines indicate first order transitions, the dashed red and blue lines indicate the spinodal lines (limits of metastability) and the black dotted line indicates a SCO. For (b,c) we set $k_1 = -0.911k_2$

S8. References

1. S. Scott, T. M. Ross, B. Moubaraki, K. S. Murray, S. M. Neville, Spin crossover in polymeric materials using Schiff base functionalized triazole ligands. *Eur. J. Inorg. Chem.*, **2013,** *5-6*, 803−812.
2. J.-F. Létard, P. Guionneau, L. Rabardel, J. A. K. Howard, A. E. Goeta, D. Chasseau, O. Kahn, Structural, magnetic, and photomagnetic studies of a mononuclear iron(II) derivative exhibiting an exceptionally abrupt spin transition. Light-induced thermal hysteresis phenomenon. *Inorg. Chem.* **1998**, *37*, 4432−4441.
3. J.-F. Létard, Photomagnetism of iron(II) spin crossover complexes—the *T*(LIESST) approach. *J. Mater. Chem.* **2006**, *16*, 2550−2559.
4. J.-F. Létard, L. Capes, G. Chastanet, N. Moliner, S. Létard, J. A, Real, O. Kahn, Critical temperature of the LIESST effect in iron(II) spin crossover compounds. *Chem. Phys. Lett.* **1999**, *313*, 115−120.
5. S. Marcen, L. Lecren, L. Capes, H. A. Goodwin, J.-F. Létard, Critical temperature of the LIESST effect in a series of hydrated and anhydrous complex salts [Fe $(bpp)_2$] X_2. *Chem. Phys. Lett.* **2002**, *358*, 87−95.
6. A. Hauser, Light-induced spin crossover and the high-spin → low-spin relaxation. Spin crossover in transition metal compounds II. *Top. Curr. Chem.* **2004**, *234*, 155−198.
7. J.-F. Létard, P. Guionneau, O. Nguyen, J. S. Costa, S. Marcén, G. Chastanet, M. Marchivie, L. Goux-Capes, A guideline to the design of molecular-based materials with long-lived photomagnetic lifetimes. *Chem. - Eur. J.* **2005**, *11*, 4582−4589.
8. K. S. Wallwork, B. J. Kennedy, D. Wang. The high-resolution powder diffraction beamline for the Australian Synchrotron. *AIP Conf. Proc.* **2007**, 879, 879−882.
9. B. Schmitt, C. Brönnimann, E. Eikenberry, F. Gozzo, C. Hörmann, R. Horisberger, B. Patterson, Mythen detector system. *Nucl. Instrum. Methods Phys. Res.*, *Sect. A*, **2003**, *501*, 267−272.
10. L. Jong, G. Ruben, K. Spear, *PDViPeR*; Synchrotron Light Source Australia *Pty Ltd*. **2014**.
11. A. Coelho, *TOPAS, Version 6*, Bruker AXS GmbH, Karlsruhe, Germany, **2007**.
12. *CrysAlisPro*, Oxford Diffraction / Agilent Technologies UK Ltd., Yarnton, Oxfordshire, England, **2014**.
13. G. M. Sheldrick, SHELXT–Integrated space-group and crystal-structure determination. *Acta Cryst. A*, **2015**, *A71*, 3−8.
14. G. M. Sheldrick, *Crystal structure refinement with SHELXL. Acta Cryst. C*, **2015**, *C71*, 3−8.
15. O. V. Dolomanov, L. J. Bourhis, R. J. Gildea, J. A. K. Howard, H. Puschmann, OLEX2: a complete structure solution, refinement and analysis program. *J. Appl. Cryst.*, **2009**, *42*, 339−341.
16. A. L. Spek, Single-crystal structure validation with the program PLATON. *J. Appl. Crystallogr.*, **2003**, 36, 7–13.
17. S. A. Moggach, D. R. Allan, S. Parsons, J. E. Warren, Incorporation of a new design of backing seat and anvil in a Merrill–Bassett diamond anvil cell. *J. Appl. Crystallogr.* **2008**, 41, 249–251.
18. G. J. Piermarini, S. Block, J. D. Barnett, R. A. Forman, Calibration of the pressure dependence of the R1 ruby fluorescence line to 195 kbar. *J. App. Phys.*, **1975**, *46*, 2774−2780.